Electrochemical synergies of heterostructured Fe$_2$O$_3$-MnO redox couple for oxygen evolution reaction in alkaline water splitting

Junyeong Kim, Jun Neoung Heo, Jeong Yeon Do*, Rama Krishna Chava, Misook Kang*

Department of Chemistry, College of Natural Sciences, Yeungnam University, Gyeongsan, Gyeongbuk 38541, Republic of Korea

*Corresponding author: Tel: +82-53-810-3798, Fax: +82-53-815-5412, daengi77@ynu.ac.kr (J. Y. Do); Tel: +82-53-810-2363, Fax: +82-53-815-5412, mskang@ynu.ac.kr (M. Kang)

Abstract

For efficient electrode development in an electrolysis system, Fe$_2$O$_3$, MnO, and heterojunction Fe$_2$O$_3$-MnO materials were synthesized via a simple sol-gel method. These particles were coated on a Ni-foam electrode, and the resulting material was used as an electrode to be used during an oxygen evolution reaction (OER). A 1000-cycle OER test in a KOH alkaline electrolyte indicated that the heterojunction Fe$_2$O$_3$-MnO/NF electrode exhibited the most stable and highest OER activity: it exhibited a low overvoltage (n) of 370 mV and a small Tafel slope of 66 mV/dec. X-ray photoelectron spectroscopy indicated that the excellent redox performance contributed to the synergy of Mn and Fe, which enhanced the OER performance of the Fe$_2$O$_3$-MnO/NF electrode. Furthermore, the effective redox reaction of Mn and Fe indicated that the structure maintained stability even under 1000 repeated OER cycles.

Keywords: Heterostructured Fe$_2$O$_3$-MnO; Oxygen evolution reaction; Alkaline water splitting; Electrochemical synergy

1. Introduction

Hydrogen has the highest energy density per unit mass and is known as a clean energy source that does not emit any exhaust gas except for water when used as fuel. Although significant amounts of H_2 have been produced through the modification of fossil fuels [1], global warming and depletion of fossil fuels have recently led to attempts to obtain H_2 via new conversion methods in various countries around the world. In particular, the method of electrolyzing water to produce H_2 is an innovative and ecofriendly technology because it uses the cleanest and abundant resource on earth—water—as a raw material for H_2 [2]. The water electrolysis reaction, which is described by $2H_2O \leftrightarrow H_2 + O_2$, consists of two half reactions: the hydrogen evolution reaction (HER) and the oxygen evolution reaction (OER) [3]. HERs are one-electron reactions, and catalysts that exhibit excellent activity have been reported because of the relatively simple mechanism of the reaction: Pt electrodes with a high reduction potential are widely used [4], and in recent years, C-doped electrodes with excellent conductivity, such as graphene, have been introduced [5]. In contrast, the OERs are four-electron reactions, and the reaction mechanism is complex; many overvoltages are required in the O_2-generating reaction [6]. Noble-metal oxides such as RuO_2 [7] and IrO_2 [8] have been used as ideal catalysts. However, owing to the scarcity and high price of the metals, there is a definite limit to industrial applications in which a large area is required. Therefore, to produce H_2 electrochemically, it is essential to develop an OER catalyst that is inexpensive and has a high efficiency for electrolysis.

In this study, we combined two particles with different structures to design an electrochemical OER catalyst for the efficient electrolysis of water. In recent years, heterojunction particles have exhibited various properties at the junction interface, such as an

increase in the amount of surface active sites, electron-rich interface formation, effective charge separation, and suppression of exciton recombination; consequently, they have led to performance improvements in various application fields [9–11]. We considered the following three points for designing the OER electrode material: 1) the position of the bandgap of the two heterojunction bands was arranged to facilitate the flow of electrons; 2) the voltage in the heterojunction particles was maintained above 1.2 V; and 3) the active metals of the heterojunction particles were configured to have a redox reaction, taking into account the reduction potential. The redox couple metals were investigated considering the reduction potential of the active metal, and the electron transport was facilitated by the heterojunction particles made of these redox couples. The redox couple metals selected in this study were Fe and Mn, which are the most inexpensive and abundant transition metals present in Earth's crust. The metal oxides Fe_2O_3 and MnO were mixed, and the resulting material was used as an efficient, durable, and ecofriendly electrode catalyst for water electrolysis. During water electrolysis, it was expected that the redox reaction would proceed on its own—the ferrous metal with a slightly reduced potential is reduced to $Fe^{3+} \rightarrow Fe^{2+}$, $E_0 = 0.77$ V, while the Mn is oxidized to $Mn^{2+} \rightarrow Mn^{3+}$ ($Mn^{2+} \rightarrow Mn^0$, $E_0 = -1.18$ V, too difficult)—and that the electronic cycle would be maintained continuously [12]. Pure Fe_2O_3 and MnO were synthesized via the sol-gel method, which is the simplest synthesis method, and an Fe_2O_3-MnO hetero-mixture grafted with the two oxides was also synthesized via the sol-gel method. Subsequently, the two types of metal-oxide powders were dispersed/coated on Ni foam (NF) to fabricate the final electrode. The objective of this study was to evaluate the synergy of Fe and Mn as a redox couple.

2. Experimental

2.1. Synthesis of MnO, Fe₂O₃, and Fe₂O₃-MnO materials

MnO and Fe₂O₃ materials were prepared via the typical sol-gel method, as follows.
For the synthesis of MnO, 4.0 g of manganese dichloride tetrahydrate ($MnCl_2 \cdot 4H_2O$, ≥97%,
Sigma-Aldrich.com) was dissolved in 100 mL of distilled (DI) water with stirring for
approximately 2 h. The resulting homogeneous mixture was heated at 70 °C for 4 h to evaporate
the DI water solvent and obtain a brown precipitate. The resulting precipitate was washed
several times with water and ethanol alternately and dried overnight at 70 °C. MnO crystalline
catalysts were finally synthesized via sintering at 500 °C for 4 h in an Ar gas atmosphere to
prevent the Mn from being oxidized into trivalent or tetravalent ions.

Fe₂O₃ was prepared via a similar procedure. First, 6.0 g of ferric chloride hexahydrate
($FeCl_3 \cdot 6H_2O$, ≥99%, Sigma-Aldrich.com) was dissolved in 100 mL of DI water. After
approximately 2 h of stirring, ammonia water (NH_4OH, ≥25% NH_3 in H_2O, Sigma-
Aldrich.com) was added dropwise until the pH of the solution was 8.0. The orange precipitate
was washed several times with DI water and ethanol and dried overnight at 70 °C. The resulting
powder was sintered at 500 °C for 4 h to produce an Fe₂O₃ crystalline catalyst.

Finally, the heterojunction Fe₂O₃-MnO material was prepared via impregnation, as
follows. The prepared crystalline Fe₂O₃ and MnO were mixed with absolute ethanol
(CH_3CH_2OH, ≥99.8%, Sigma-Aldrich.com) at a weight ratio of 1:1, followed by stirring for 2
h to obtain a homogeneous solution. Then, a red-brown-colored powder was obtained through
evaporation at 70 °C. The obtained powder was heat-treated at 400 °C for 3 h in an Ar
atmosphere to produce the heterojunction Fe₂O₃-MnO crystal.

2.2. Fabrication of MnO/NF, Fe₂O₃/NF, and Fe₂O₃-MnO/NF electrodes

The electrodes for OER were prepared as follows in **Scheme 1a**: The surface was treated with 5.0% HCl for approximately 30 min to remove surface impurities on the substrate, i.e., NF (1.0 cm × 1.0 cm). The surface of the NF was then washed with DI water and absolute ethanol and dried at room temperature. The coating solution was prepared by mixing 30 mg of the synthesized catalyst powder (MnO, Fe_2O_3, and Fe_2O_3-MnO) with 600 μL of ultrapure water, 600 μL of absolute ethanol, and 60 μL of a 5.0 wt.% Nafion solution (Sigma-Aldrich.com), followed by dispersion for 3 h. The coating solution was evenly coated onto the surface-treated NF using a dip-coating method and then dried at 70 °C. Subsequently, MnO/NF, Fe_2O_3/NF, and Fe_2O_3-MnO/NF electrodes were prepared via heat treatment at 200 °C for 3 h.

2.3. Characterizations

The crystal structures of the MnO, Fe_2O_3, and Fe_2O_3-MnO electrodes were examined via X-ray diffraction (XRD) analysis (Miniflex, Rigaku) using Ni-filtered CuKα radiation (30.0 kV, 15.0 mA) in the 2θ range of 20°–90°. The surface morphology of the particles was observed using a Hitachi S-4100 field-emission scanning electron microscope. Energy-dispersive X-ray spectroscopy (EDS) and EDS elemental mapping of the particles were performed using EDAX (EX-250, Horiba). Transmission electron microscopy (TEM) was performed using an H-7600 (Hitachi) instrument. X-ray photoelectron spectroscopy (XPS) was performed using an AXIS-NOVA (Kratos Inc.) equipped with AlKα (1486.6 eV) radiation.

2.4. Electrochemical measurements

All electrochemical measurements were performed at room temperature (25 °C) using

an electrochemical cell test system and IVIUMnSTAT (Ivium Technologies, The Netherlands). The electrochemical OER activity was tested in an alkaline electrolyte (1 M KOH, pH = 14) using a standard electrochemical device (**Scheme 1b**): MnO/NF, Fe_2O_3/NF, and Fe_2O_3-MnO/NF were used as the working electrode, and Hg/Hg_2Cl_2 (saturated calomel electrode, SCE) and Pt wire were used as the reference and counter electrodes, respectively. The measured potential was converted into the potential of a reversible hydrogen electrode (V_{RHE}) using the following calibration equation [13].

$$V_{RHE} = V_{SCE} + 0.241 + 0.059 \times pH$$

For the initial stabilization of the electrode, 100 cycles of cyclic voltammetry (CV) scans (50.0 mV/s) were performed at approximately 1.0–1.7 V (vs. RHE). Linear sweep voltammetry (LSV) was performed at a scan rate of 5.0 mV/s in 1 M KOH.

3. Result and Discussion

Figs. 1A and **B** show the XRD pattern and TEM image of the powder particles before the electrode assembly. The XRD pattern of MnO is consistent with the cubic structure with the Fm-3 space group, and the peaks corresponding to the (111), (200), and (220) diffraction planes are observed at $2\theta = 34°$, $40°$, and $58°$, respectively (JCPDS card no. 01-072-1533) [14]. The XRD peaks of Fe_2O_3 correspond to the diffraction planes attributed to the rhombohedral structure of the R-3c spatial group and were observed at $2\theta = 24°$ (012), $33°$ (104), $35°$ (110), and $40°$ (JCPDS card no. 01-089-0598) [15]. The heterojunction Fe_2O_3-MnO particles exhibited the crystal-structure patterns of both MnO and Fe_2O_3. Unexpectedly, the intensity of the XRD peaks was increased overall for the heterojunction Fe_2O_3-MnO particles. This may be

due to the further growth of crystals during the sintering process for grafting the two types of pure crystals. The peak corresponding to Fe_2O_3 was more distinct, suggesting that the Fe_2O_3 crystals entirely covered the MnO crystals. This is confirmed by the TEM image in Figure 1B: the MnO sample exhibited a broad and thin sheet shape (approximately 400–500 nm thick), and in the Fe_2O_3 sample, a thin cloth piece of approximately 100 nm was rounded to a 15 × 100 nm rod shape. Eventually, it appeared similar to a petal. In the heterojunction Fe_2O_3-MnO sample, a piece of Fe_2O_3 covered the MnO sheet, which is consistent with the XRD results.

Fig. 2A shows the results of EDS analysis of selected surfaces of the film-type electrodes assembled using the manufactured powders. According to the EDS analysis results, the atomic ratio of Mn:O on the surface of MnO was approximately 1.0:1.2, and the atomic ratio of Fe:O on the Fe_2O_3 surface was approximately 2.0:3.3. This indicates that the metals were stoichiometrically contained in the particles and that the metal oxides were manufactured reliably. In the case of Fe_2O_3-MnO, the ratio of Mn:Fe:O was 1.2:1.0:5.5, although it was physically grafted. **Fig. 2B** shows a scanning electron microscopy (SEM) image of the surface of the electrode coated with catalyst particles on the NF substrate. Regardless of the type of catalyst, the catalyst uniformly covered the NF. Compared with the powder catalyst form in Fig. 1, the catalyst was evenly coated on the NF in its original shape, without deformation. **Fig. 2C** shows the element mapping of the electrode surface, confirming that Mn, O_f, and Fe were uniformly distributed. The intensity of the color is proportional to the concentration of the element, and the color intensity changes stoichiometrically. In particular, the color of Fe in the Fe_2O_3-MnO heterojunction is similar to that of Fe_2O_3, indicating that the Fe_2O_3 crystal covered the surface of MnO, which agrees with the results of XRD and TEM.

Fig. 3 shows CV curves obtained when NF, MnO/NF, Fe_2O_3/NF, and Fe_2O_3-MnO/NF samples were used as the working electrode. Generally, NFs exhibit characteristic oxidation

and reduction peaks of Ni at 1.4 and 1.3 V [16]. Repeated CV tests for 100 cycles were performed to evaluate the stability of the electrodes for oxidation–reduction. As the number of CV scans increased, the oxidation and reduction peaks of the Ni foil were shifted to a positive voltage. In general, it has been reported that the oxidation–reduction peak shifts to a positive voltage value until a stable phase is obtained on the surface of the NF in the OER and that it takes approximately 100 cycles for the peaks to stabilize [17]. However, no potential change was observed in the MnO/NF, Fe_2O_3/NF, and Fe_2O_3-MnO/NF electrodes assembled here, despite cycling. This indicates that the MnO, Fe_2O_3, and Fe_2O_3-MnO catalysts formed a stable structure at the beginning, suggesting that they contributed to the activity of the catalyst. Notably, for the heterojunction Fe_2O_3-MnO catalyst, no peak change was observed during the 100 cycles, and the current density was more stable than those of the other two samples. This indicates that the MnO and the Fe_2O_3 particles were very stable and strongly bonded to each other; thus, there was little loss of catalytic active sites. The current density and peak area in the CV curve are closely related to the reversible redox reaction and the electrical active surface area [18]. In all NF-based catalysts, the peak area is expanded by increasing the volume of $Ni(OH)_2$/NiOOH with cyclic repetition according to the following equations [19].

$$Ni^0 + 2OH \rightarrow Ni(OH)_2 + 2e^-$$

$$Ni(OH)_2 \leftrightarrow NiOOH + e^- + H^+$$
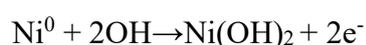
Furthermore, the overall current-density range for the NF electrode coated with the catalyst was significantly increased compared with that of pure NF, which may be related to the catalytic activity. A uniformly dispersed metal or metal oxide has been reported to provide a large number of active sites in the electrocatalytic reaction, resulting in a significant increase in the current density [20]. Both the current density and the peak area of the heterojunction Fe_2O_3-MnO/NF electrodes were significantly increased. This is presumably due to the

excellent redox performance of Mn and Fe, and it is expected that the junction of the heterojunction structure generated more active sites and had a high electron density to promote electron transfer during the catalytic reaction [21].

The LSV curves were measured at the 100-cycle OER test. The results are shown in **Fig. 4A**. In general, the activity of electrocatalysts is compared according to the overvoltage at a current density of 10 mA/cm^2 in a water electrolysis reaction [22]. For a pure NF electrode, an overvoltage (η) of 430 mV was needed to reach a current density of 10 mA/cm^2. In contrast, the MnO/NF and Fe$_2$O$_3$/NF electrodes exhibited relatively low over-voltages of 410 and 400 mV, respectively, indicating that they had better activity than the pure NF. The heterojunction Fe$_2$O$_3$-MnO/NF exhibited an overvoltage of 370 mV, confirming that it had the best OER activity among the electrodes examined in this study. **Fig. 4B** shows the Tafel slopes derived from the LSV polarization curves. The Tafel slope indicates the inherent characteristics of electrocatalysts, and a smaller Tafel slope corresponds to better water oxidation reaction kinetics [23]. As shown in Fig. 4B, the Tafel slope for the Fe$_2$O$_3$-MnO/NF electrode was 66 mV/dec, which was significantly smaller than those for the NF (100 mV/dec), MnO/NF (74 mV/dec), and Fe$_2$O$_3$/NF (78 mV/dec) electrodes.

Figs. 5A and **5B** show the LSV curves at 1000 cycle for the OER and SEM images of the electrode surface before and after the 1000 cycled OER when the heterojunction Fe$_2$O$_3$-MnO/NF was used as the working electrode. Surprisingly, when the Fe$_2$O$_3$-MnO/NF electrodes were used, the LSV curve retained its performance as early as in the 1000-cycle OER test. The Tafel plots obtained after 1000 cycles exhibited negligible slope differences, indicating that the Fe$_2$O$_3$-MnO/NF electrode had very good durability. **Fig. 5B** shows an SEM image of the Fe$_2$O$_3$-MnO/NF electrode surface before and after 1000 cycles in the OER. On the surface of the NF electrode after the OER, the Fe$_2$O$_3$-MnO heterojunction particles were well attached equally

before the reaction, and they surprisingly had a similar size and shape to the fresh Fe_2O_3-MnO particles. This is presumably because the heterojunction structure was well maintained owing to the self-redox reaction of Mn and Fe, which facilitated the electron transfer, and the voltage application did not damage the NF electrode as a substrate.

Fig. 6 shows the XPS results of Fe2p, Mn2p, Ni2p, and O1s for the Fe_2O_3-MnO/NF electrode after the OER. An $Ni2p_{3/2}$ peak corresponding to metal Ni appeared at 852.6 eV, and an $Ni2p_{3/2}$ peak corresponding to Ni^{2+} appeared at 855–856 eV [24]. Unfortunately, no complete metal-Ni component was observed in the NF electrode before the OER. This is evidence that the NF was partially oxidized during the process of coating the particles on the NF. Perhaps the OER performance could have been improved if the NF used as the substrate electrode had maintained a perfect metal state. However, only the $Ni2p_{3/2}$ highest occupied molecular orbital peak attributed to Ni^{2+} was broadly observed at 856.1 eV for NF before the reaction (fortunately, NF was not completely oxidized to NiO, as lowest unoccupied molecular orbital (LUMO) moiety was not observed). After the OER, the binding energy shifted slightly to a higher value (856.4 eV), and the peak shape changed sharply. Furthermore, the $Ni2p_{1/2}$ peak corresponding to the LUMO was observed at 874.1 eV after the reaction. This indicates that some of the Ni in the NF was oxidized to Ni^{2+} during the OER. The $Fe2p_{3/2}$ peak for fresh Fe_2O_3-MnO/NF was separated into peaks in various oxidation states, and peaks attributed to Fe^0, Fe^{2+}, and Fe^{3+} were observed at binding energies of 706.4, 708.5, and 711.2 eV, respectively [25]. Additionally, the $Fe2p_{1/2}$ peak corresponding to Fe^{3+} was observed at 724.9 eV. The observation of Fe^0 and Fe^{2+} in the XPS analysis indicates that the Fe^{3+} accepted electrons from the NF, becoming reduced and oxidizing the NF, during the loading of the Fe_2O_3-MnO particles onto the NF. However, after the OER, the isolated peaks converged to one peak at 711.2 eV. This suggests that the oxidation state of Fe during the OER was stable at 3+ [26]. In the high-resolution Mn2p XPS spectrum obtained before the OER, two main

spin-orbitals corresponding to Mn2p$_{3/2}$ and Mn2p$_{1/2}$ (indicating the presence of Mn^{2+}) were observed at 641.6 and 653.6 eV, respectively [27]. Additionally, the Mn2p$_{3/2}$ peak attributed to Mn^{3+} exhibited a low binding energy (644.7 eV). After the OER, the Mn2p$_{3/2}$ peak corresponding to Mn^{2+} converged at 641.6 eV as a single peak, the intensity of the peak decreased, and the peak width increased, similar to the results for Fe2p. This indicates that the oxidation state of Mn was stabilized to 2+ during the OER. According to the XPS results for Fe2p and Mn2p, the active metals that constituted the electrode during the OER were reduced to Fe$^{3+} \rightarrow$ Fe^{2+} (Mn$^{2+} \rightarrow$ Mn^{3+}) when charged, and the electrons moved in the opposite direction during discharging. At this time, redox couples were formed between Fe^{3+} and Mn^{2+}, and they were repeatedly oxidized–reduced and then restored. We confirmed that their redox reaction was fairly stable and that the OER performance continued to be maintained after 1000 cycles, indicating a synergy caused by the coexistence of Mn and Fe. Before the OER, the XPS spectra of O1s were separated by various binding energies at 529.9, 531.9, and 533.8 eV, which can be attributed to M-O, H$_2$Oads, and M-OH, respectively [28]. After the OER, the peaks were slightly shifted to higher binding energies. The H$_2$Oads peak due to adsorbed water was stronger than the M-O peak corresponding to O$_2$ in the lattice. This is because during the OER, when the active metals underwent repeated oxidation–reduction reactions, a part of the M-O bond of the lattice was broken. However, this did not appear to be a major factor affecting the oxidation state of Mn or Fe; rather, it may have been related to the partially damaged NF electrode.

4. Conclusion

Fe$_2$O$_3$ and MnO were synthesized via a sol-gel method, and an Fe$_2$O$_3$-MnO heterojunction mixture was prepared. These particles were coated onto NF electrodes, and the electrochemical properties of the resulting materials were evaluated. XRD patterns and TEM images of the powder particles were analyzed to confirm their crystallinity and shape. Through SEM and elemental mapping of the NF surface after a 1000-cycle OER test, the adhesion degree of the particles on the NF was examined. The change in and stability of the oxidation state of the active metals were determined based on the XPS spectra before and after the OER. As a result of the OER, a lower overvoltage (1.60 V/10 mAcm^{-2}) was obtained for the Fe$_2$O$_3$-MnO/NF (containing the heterojunction of the two oxides) than for the pure Fe$_2$O$_3$/NF and MnO/NF, and the Tafel slope for the heterojunction electrode was as small as 66 mV/dec. Even after 1000 cycles, the OER performance of Fe$_2$O$_3$-MnO/NF remained stable, without deterioration. These results indicate that during Mn and Fe self-redox reactions in Fe$_2$O$_3$-MnO/NF hetero-electrodes, the Mn oxidizes O$_2$ in water and the Fe reduces H$_2$, facilitating the migration of electrons. Eventually, it appears that this is a synergistic effect in the OER.

Acknowledgements

References

References

1. Hisatomi, T.; Domen, K. Reaction systems for solar hydrogen production via water splitting with particulate semiconductor photocatalysts. Nat. Catal. 2019, 2, 387-399.

2. Yan, H.; Xie, Y.; Wu, A.; Cai, Z.; Wang, L.; Tian, C.; Zhang, X.; Fu, H. Anion-Modulated HER and OER Activities of 3D Ni–V-Based Interstitial Compound Heterojunctions for High-Efficiency and Stable Overall Water Splitting. Adv. Mater. 2019, 31, 1901174-1901182.

3. Bu, X.; Wei, R.; Gao, W.; Lan, C.; Ho, J.C. A unique sandwich structure of a CoMnP/Ni2P/NiFe electrocatalyst for highly efficient overall water splitting. J. Mater. Chem. A 2019, 7, 12325-12332.

4. Roger, I.; Shipman, M.A.; Symes, M.D. Earth-abundant catalysts for electrochemical and photoelectrochemical water splitting. Nat. Rev. Chem. 2017, 1, 1-14.

5. Hou, Y.; Lohe, M.R.; Zhang, J.; Liu, S.; Zhuang, X.; Feng, X. Vertically oriented cobalt selenide/NiFe layered-double-hydroxide nanosheets supported on exfoliated graphene foil: an efficient 3D electrode for overall water splitting. Energy Environ. Sci. 2016, 9, 478-483.

6. Wang, W.; Xu, X.; Zhou, W.; Shao, Z. Recent Progress in Metal-Organic Frameworks for Applications in Electrocatalytic and Photocatalytic Water Splitting. Adv. Sci. 2017, 4, 160037-1600391.

7. Liu, J.; Zheng, Y.; Jiao, Y.; Wang, Z.; Lu, Z.; Vasileff, A.; Qiao, S. NiO as a Bifunctional Promoter for RuO 2 toward Superior Overall Water Splitting. Small (Weinheim an der Bergstrasse, Germany) 2018, 14, 1-10.

8. Yu, F.; Zhou, H.; Huang, Y.; Sun, J.; Qin, F.; Bao, J.; Goddard, 3., William A; Chen, S.; Ren, Z. High-performance bifunctional porous non-noble metal phosphide catalyst for overall water splitting. Nat. Commun. 2018, 9, 2551-2559.

9. Wu, A.; Xie, Y.; Ma, H.; Tian, C.; Gu, Y.; Yan, H.; Zhang, X.; Yang, G.; Fu, H. Integrating the active OER and HER components as the heterostructures for the efficient overall water splitting. Nano Energy 2018, 44, 353-363.

10. Zhu, C.; Wang, A.; Xiao, W.; Chao, D.; Zhang, X.; Tiep, N.H.; Chen, S.; Kang, J.; Wang, X.; Ding, J.; Wang, J.; Zhang, H.; Fan, H.J. In Situ Grown Epitaxial Heterojunction Exhibits

High-Performance Electrocatalytic Water Splitting. Adv. Master. 2018, 30, 170551-170523.

11. Ouyang, T.; Ye, Y.; Wu, C.; Xiao, K.; Liu, Z. Heterostructures Composed of N-Doped Carbon Nanotubes Encapsulating Cobalt and β-Mo2 C Nanoparticles as Bifunctional Electrodes for Water Splitting. Angew. Chem. Int. Ed. 2019, 58, 4923-4928.

12. Peng, X.; Qu, J.; Tian, S.; Ding, Y.; Hai, X.; Jiang, B.; Wu, M.; Qiu, J. Green fabrication of magnetic recoverable graphene/MnFe2O4 hybrids for efficient decomposition of methylene blue and the Mn/Fe redox synergetic mechanism. RSC Adv. 2016, 6, 104549-104555.

13. Choi, S.Y.; Kim, C.; Han, D.S.; Park, H. Facilitating hole transfer on electrochemically synthesized p-type CuAlO2 films for efficient solar hydrogen production from water. J. Master. Chem. A 2017, 5, 10165-10172.

14. Qiu, D.; Ma, L.; Zheng, M.; Lin, Z.; Zhao, B.; Wen, Z.; Hu, Z.; Pu, L.; Shi, Y. MnO nanoparticles anchored on graphene nanosheets via in situ carbothermal reduction as high-performance anode materials for lithium-ion batteries. Mater. Lett. 2012, 84, 9-12.

15. Tadic, M.; Panjan, M.; Damnjanovic, V.; Milosevic, I. Magnetic properties of hematite (α-Fe2O3) nanoparticles prepared by hydrothermal synthesis method. Appl. Surf. Sci. 2014, 320, 183-187.

16. Shalom, M.; Ressnig, D.; Yang, X.; Clavel, G.; Fellinger, T.P.; Antonietti, M. Nickel nitride as an efficient electrocatalyst for water splitting. J. Master. Chem. A 2015, 3, 8171-8177.

17. Huang, C.; Zou, Y.; Ye, Y.; Ouyang, T.; Xiao, K.; Liu, Z. Unveiling the active sites of Ni-Fe phosphide/metaphosphate for efficient oxygen evolution under alkaline conditions. Chem. Commun. 2019, 55, 7687-7690.

18. Ullah, N.; Zhao, W.; Lu, X.; Oluigbo, C.J.; Shah, S.A.; Zhang, M.; Xie, J.; Xu, Y. In situ growth of M-MO (M = Ni, Co) in 3D graphene as a competent bifunctional electrocatalyst for OER and HER. Electrochim. Acta 2019, 298, 163-171.

19. Urso, M.; Torrisi, G.; Boninelli, S.; Bongiorno, C.; Priolo, F.; Mirabella, S. Ni(OH)2@Ni core-shell nanochains as low-cost high-rate performance electrode for energy storage applications. Sci. Rep. 2019, 9, 1-11.

20. Moosavifard, S.E.; Shamsi, J.; Fani, S.; Kadkhodazade, S. 3D ordered nanoporous NiMoO4 for high-performance supercapacitor electrode materials. RSC Adv. 2014, 4, 52555-52561.

21. Li, X.; Antonietti, M. Metal nanoparticles at mesoporous N-doped carbons and carbon nitrides: functional Mott–Schottky heterojunctions for catalysis. Chem. Soc. Rev. 2013, 42, 6593-6604.

22. Liang, H.; Gandi, A.N.; Xia, C.; Hedhili, M.N.; Anjum, D.H.; Schwingenschlögl, U.; Alshareef, H.N. Amorphous NiFe-OH/NiFeP Electrocatalyst Fabricated at Low Temperature for Water Oxidation Applications. ACS Energy Lett. 2017, 2, 1035-1042.

23. Han, A.; Chen, H.; Sun, Z.; Xu, J.; Du, P. High catalytic activity for water oxidation based on nanostructured nickel phosphide precursors. Chem. Commun. 2015, 51, 11626-11629.

24. Xu, T.; Li, G.; Zhao, L. Ni-Co-S/Co(OH)2 nanocomposite for high energy density all-solid-state asymmetric supercapacitors. Chem. Eng. J. 2018, 336, 602-611.

25. Wang, Y.; Liu, D.; Liu, Z.; Xie, C.; Huo, J.; Wang, S. Porous cobalt–iron nitride nanowires as excellent bifunctional electrocatalysts for overall water splitting. Chem. Commun. 2016, 52, 12614-12617.

26. Zhang, C.; Zhang, C.; Xie, Y.; Deng, H.; Su, J.; Dong, Y.; Lin, J. Ternary nickel iron phosphide supported on nickel foam as a high-efficiency electrocatalyst for overall water splitting. Int. J. Hydrogen. Energy 2018, 43, 7299-7306.

27. Li, X.; Xin, M.; Guo, S.; Guo, W.; Cai, T.; Du, D.; Xing, W.; Zhao, L.; Xue, Q.; Yan, Z. Insight of synergistic effect of different active metal ions in layered double hydroxides on their electrochemical behaviors. Electrochim. Acta 2017, 253, 302-310.

28. Luo, Z.; Miao, R.; Huan, T.D.; Mosa, I.M.; Poyraz, A.S.; Zhong, W.; Cloud, J.E.; Kriz, D.A.; Thanneeru, S.; He, J.; Zhang, Y.; Ramprasad, R.; Suib, S.L. Mesoporous MoO3–x Material as an Efficient Electrocatalyst for Hydrogen Evolution Reactions. Adv. Energy Master. 2016, 6, 160052-1600538.

Figure captions

Scheme 1. Electrode fabrication sequence (a) and electrochemical device image for OER test (b).

Fig. 1. XRD patterns (A) and TEM images (B) of the powder particles before the electrode assembly.

Fig. 2. EDS analysis of selected surfaces of the film-type electrodes (A), and the images of scanning electron microscopy (SEM) (B) and element mapping on the surface of the electrode (C).

Fig. 3. CV curves obtained when NF, MnO/NF, Fe_2O_3/NF, and Fe_2O_3-MnO/NF samples were used as the working electrode.

Fig. 4. LSV curves measured at the 100-cycle OER test (A) and Tafel slopes derived from the LSV polarization curves (B).

Fig. 5. LSV curves at 1000 cycle for the OER (A) and SEM images of the electrode surface before and after the 1000 cycled OER (B).

Fig. 6. XPS curves of Fe2p, Mn2p, Ni2p, and O1s for the Fe_2O_3-MnO/NF electrode after the OER.
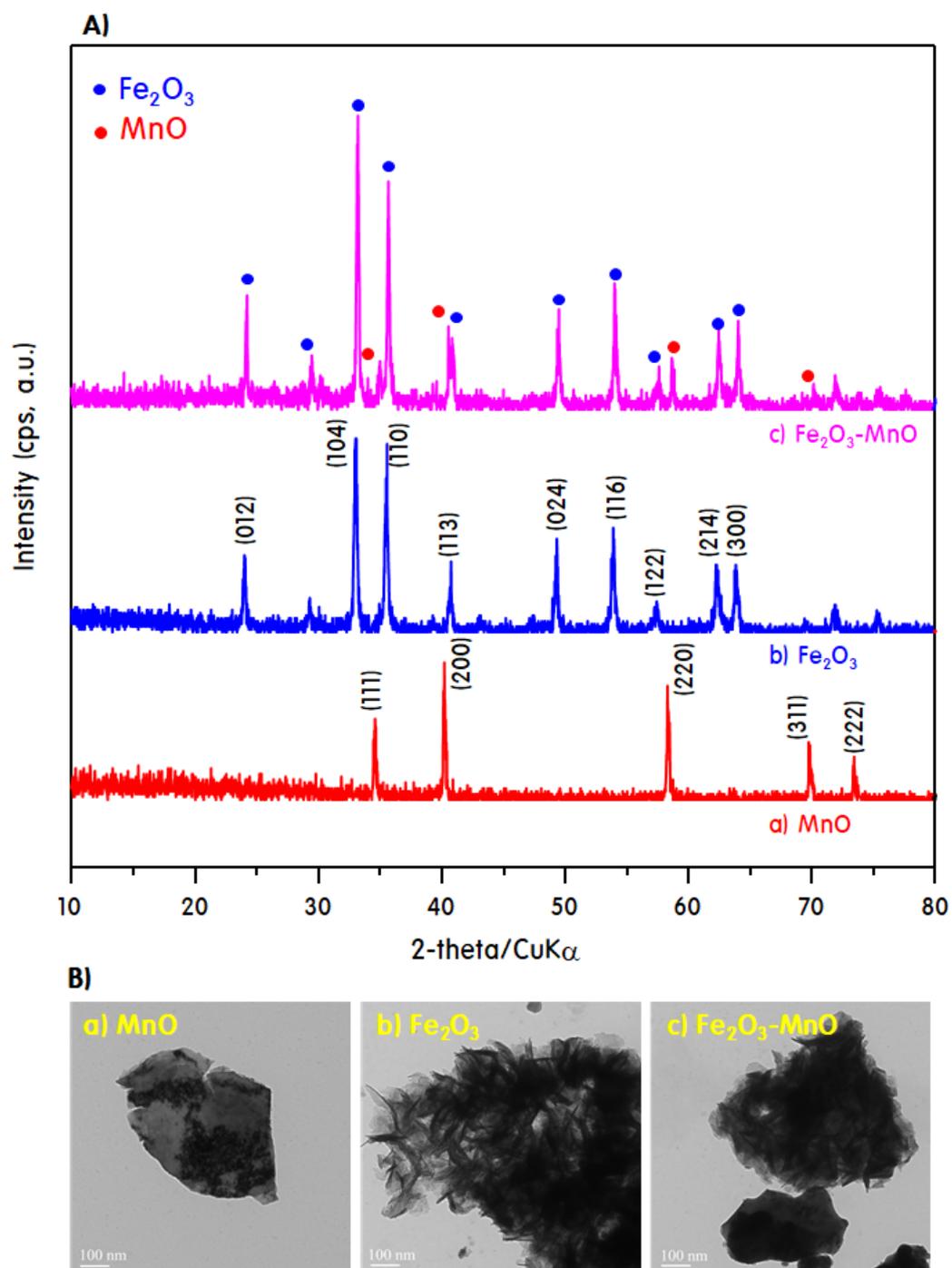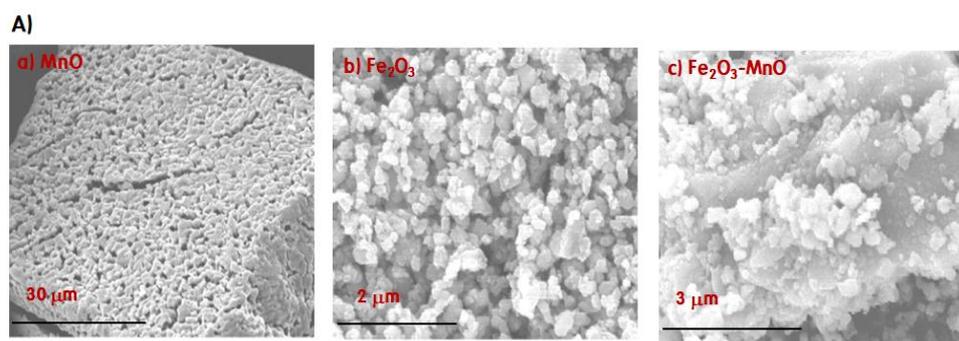
Scheme 1
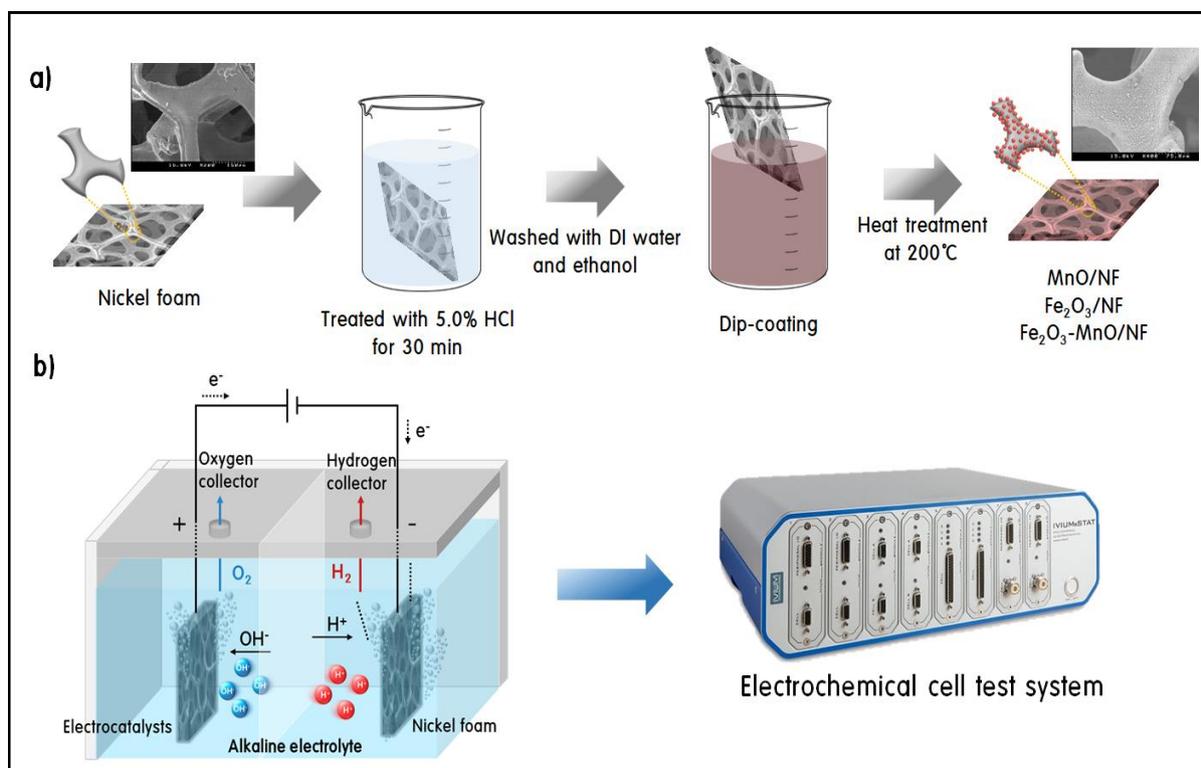
Fig. 1

Fig. 2

Catalysts	Atomic compositions on the surface of catalysts		
	Mn	Fe	O
MnO	45.51	-	54.49
Fe$_2$O$_3$	-	33.53	66.47
Fe$_2$O$_3$-MnO	15.30	13.29	71.40

Fig. 3

Fig. 4

Fig. 5

Fig. 6